Soft Matter

PAPER

View Article Online
View Journal | View Issue

Cite this: *Soft Matter*, 2016, 12, 2288

Hydrogen bonding strength of diblock copolymers affects the self-assembled structures with octa-functionalized phenol POSS nanoparticles

Yi-Syuan Lu, Chia-Yu Yu, Yung-Chih Lin and Shiao-Wei Kuo*

Received 7th December 2015,
Accepted 2nd January 2016

DOI: 10.1039/c5sm02959g

www.rsc.org/softmatter

In this study, the influence of the functional groups by the diblock copolymers of poly(styrene-*b*-4-vinylpyridine) (PS-*b*-P4VP), poly(styrene-*b*-2-vinylpyridine) (PS-*b*-P2VP), and poly(styrene-*b*-methyl methacrylate) (PS-*b*-PMMA) on their blends with octa-functionalized phenol polyhedral oligomeric silsesquioxane (OP-POSS) nanoparticles (NPs) was investigated. The relative hydrogen bonding strengths in these blends follow the order PS-*b*-P4VP/OP-POSS > PS-*b*-P2VP/OP-POSS > PS-*b*-PMMA/OP-POSS based on the Kwei equation from differential scanning calorimetry (DSC) and Fourier transform infrared spectroscopic analyses. Small-angle X-ray scattering and transmission electron microscopic analyses show that the morphologies of the self-assembly structures are strongly dependent on the hydrogen bonding strength at relatively higher OP-POSS content. The PS-*b*-P4VP/OP-POSS hybrid complex system with the strongest hydrogen bonds shows the order–order transition from lamellae to cylinders and finally to body-centered cubic spheres upon increasing OP-POSS content. However, PS-*b*-P2VP/OP-POSS and PS-*b*-PMMA/OP-POSS hybrid complex systems, having relatively weaker hydrogen bonds, transformed from lamellae to cylinder structures at lower OP-POSS content (<50 wt%), but formed disordered structures at relatively high OP-POSS contents (>50 wt%).

Introduction

Self-assembled structures from diblock copolymers (BCPs), including alternating lamellae, bicontinuous gyroids, hexagonally packed cylinders and spheres, and organic/inorganic hybrid materials, constitute a new fascinating field in polymer science.[1,2] Considerable progress has been achieved in gaining a fundamental understanding of organic/inorganic hybrid systems formed from inorganic nanoparticles and block copolymers, the properties of which cannot be replicated in organic/organic block copolymers,[3–5] such as poly(styrene-*b*-dimethylsiloxane)[6,7] and poly(methyl methacrylate-*b*-methacryloyl polyhedral oligomeric silsesquioxane) diblock copolymers.[8–10] Polyhedral oligomeric silsesquioxane (POSS) with its unique cage-like structure, with *ca.* 1–3 nm nanoscale dimension nanoparticles (NPs), is often used for organic/inorganic hybrid materials.[11–14]

In addition to the preparation of organic/inorganic block copolymers, blending of inorganic nanoparticles within organic/organic diblock copolymers to form BCP/NP composites is quite interesting because of their possible applications in sensors, photonics, and nanodevices.[15–21] The self-assembled structures from diblock copolymers are strongly dependent on the degree of polymerizations (N), interaction parameters (χ), and the volume fractions (f) of the diblock copolymer segments.[2] At low values of χN, the diblock copolymer is usually phase-mixed. The possible disorder-to-order transition (DOT) may occur when χN increases. Therefore, the dispersion of nanoparticles in the diblock copolymer is in relation with the increasing enthalpy change from the creation of polymer–NP interfaces and the decreasing polymer conformational entropy.[22–25]

Generally, using compatible or miscible ligands with one of the block segments can provide the preferential segregation of NPs within the compatible or miscible block segment. For instance, the use of polystyrene (PS) or poly(2-vinylpyridine) (P2VP) homopolymer as ligand for the Au nanoparticle can mediate the distribution of Au nanoparticles in the self-assembled structure of PS-*b*-P2VP block copolymers.[26–30] Because the ligand of the NPs is chemical identical or similar to one of block segments, the enthalpically neutral NPs lead the entropic penalty, and thus lead the self-assembly structure, to disorder morphology at relatively higher NPs contents. To solve the disorder morphology problem, using strong hydrogen bonding has been widely studied for blending block copolymers with nanoparticles, thereby significantly improving miscibility

Department of Materials and Optoelectronic Science, Center for Nanoscience and Nanotechnology, National Sun Yat-Sen University, Kaohsiung, 804, Taiwan. E-mail: kuosw@faculty.nsysu.edu.tw

behavior or the swelling diblock copolymer segments without macrophase separation and order–order morphological transition.[15–21] For example, several nanoparticles such as CdS, Au, and POSS modified on their surfaces with hydroxyl or multiple hydrogen bonding functional groups are able to interact with the poly(ethylene oxide) (PEO), P4VP, and poly(vinylbenzyl thymine) (PVBT) domains of diblock copolymers. These strong intermolecular hydrogen bonds can significantly decrease the macrophase separation possibility of the nanoparticles and then favor microphase separation.[33–40] For example, in our previous study,[41] we investigated the ligand effects of POSS nanoparticles, where one is chemically similar to the PS block segment and the other has hydrogen bonding interactions with the P4VP block segment. The relatively weaker hydrophobic interaction between the aromatic group of the PS block segment and the octa-functionalized styrene silsesquioxane (OS-POSS) pushes the PS-*b*-P4VP block copolymer to possess disorder morphology at higher OS-POSS content.[41] On the contrary, the relatively stronger hydrogen bonding in OP-POSS/PS-*b*-P4VP induces order–order transition from alternating lamellae to cylinders and finally to body-centered cubic (BCC) spheres.[41]

As a result, we might expect strong hydrogen bonding interaction to enable relatively higher loadings of nanoparticles within the diblock copolymer segments. To the best of our knowledge, however, the hydrogen bonding strength influence on the self-assembly structures of diblock copolymers and nanoparticles has never been reported previously. In this study, we blend OP-POSS NPs with three well-established diblock copolymers—PS-*b*-PMMA, PS-*b*-P2VP, and PS-*b*-P4VP—formed through sequential anionic polymerization.[42] These three systems allowed us to make general predictions about how hydrogen bonding strength influences the structures of nanoparticles in block copolymers, with the goal of realizing multifunctional organic/inorganic hybrid materials. The inter-association equilibrium constants of P4VP/poly(vinyl phenol) (PVPh) (K_A = 1200), P2VP/PVPh (K_A = 598), and PMMA/PVPh (K_A = 37.4), as well as the self-association equilibrium constant (K_B = 66.8) of PVPh were determined based on the Painter–Coleman association model.[43–45] Therefore, the strengths of the hydrogen bonding interactions of P4VP, P2VP, and PMMA with OP-POSS follow the order P4VP/OP-POSS > P2VP/OP-POSS > PMMA/OP-POSS, with $K_A/K_B > 1$ for P4VP/OP-POSS and P2VP/OP-POSS and $K_A/K_C < 1$ for PMMA/OP-POSS.[42] In the present study, the miscibility behavior, intermolecular hydrogen bonding interaction and self-assembly structures of these three hybrid complex system were investigated using differential scanning calorimetry (DSC), Fourier transform infrared (FTIR) spectroscopy, small-angle X-ray scattering (SAXS), and transmission electron microscopy (TEM) analyses.

Experimental section

Materials

Styrene, 4-acetoxystyrene, 4-vinylpyridine, 2-vinypyridine, methyl methacrylate, and platinum(0)/1,3-divinyl-1,1,3,3-tetramethyldisiloxane complex solution [Pt(dvs)] were all obtained from Aldrich Chemical (USA). The diblock copolymers of PS_{216}-*b*-$P4VP_{257}$, PS_{366}-*b*-$P2VP_{220}$ and PS_{200}-*b*-$PMMA_{252}$ were all synthesized through sequential anionic polymerization as shown in Scheme 1.[42] OP-POSS (M_n = 1978 g mol^{-1}) was synthesized according to our previous studies.[46–49] Details of syntheses and characterizations of PS-*b*-P4VP, PS-*b*-P2VP, and PS-*b*-PMMA diblock copolymers are available elsewhere;[42–49] the characterization data for these materials are summarized in Table 1.

BCP/NP blend

Blending OP-POSS NPs with various weight fractions of PS-*b*-P4VP, PS-*b*-P2VP, and PS-*b*-PMMA block copolymers was carried out through solution blending. 5 wt% of the BCP/NPs blends in THF solution was stirred for 24 h and then cast on the Teflon pan. THF solvent was slowly evaporated at room temperature for 2 days and then dried in a vacuum oven at 120 °C for 2 days.

Characterization

Thermal properties of the blend samples were determined by DSC analysis using the TA Q-20 instrument; the instrument was operated at a heating rate of 20 °C min^{-1} from 90 °C to 200 °C under N_2; the weight of each blend sample was *ca.* 5–10 mg. FTIR spectra of blend samples were obtained using the conventional KBr disk method with the Bruker Tensor 27 FTIR spectrophotometer at room temperature. SAXS was performed using the NANOSTAR U small-angle X-ray scattering system (Bruker AXS, Karlsruhe, Germany) and Cu-K_α radiation (30 W, 50 kV, 600 mA). TEM observations were conducted using a JEOL 2100 microscope (Japan) operated at 200 kV. Ultrathin samples were prepared using the Leica Ultracut S microtome equipped with a diamond knife. The TEM images of BCP/NPs π thin film were recorded without any stain because the dark region corresponded to POSS-rich domain because the Si atoms of POSS provides the relatively higher mass contrast compared with the organic domains. The bright region corresponds to the PS phase in the minor domain, as would be expected.

Results and discussion

Thermal analyses

Fig. 1 presents DSC analyses of PS-*b*-P4VP/OP-POSS, PS-*b*-P2VP/OP-POSS, and PS-*b*-PMMA/OP-POSS blends with various compositions. Clearly, the glass transition temperature of the pure OP-POSS NP is *ca.* 18 °C[46] and the pure PS-*b*-P4VP block copolymer displays two glass transition temperatures at 106 °C and 152 °C, corresponding to PS and P4VP block segment, respectively.[41] The pure PS-*b*-P2VP diblock copolymer displayed only a single glass transition temperature of approximately 108 °C, as might be expected because pure PS and pure P2VP both display similar glass transition temperatures near this value.[50] In contrast, the pure PS-*b*-PMMA diblock copolymer also experienced two glass transition temperatures: a lower value of T_g near 116 °C (resulting from the PS segments) and a higher value near 135 °C (resulting from the PMMA segments), which is higher than pure PMMA homopolymer (*ca.* 100 °C), as has also been discussed in a previous study.[51] Notably, the T_g value

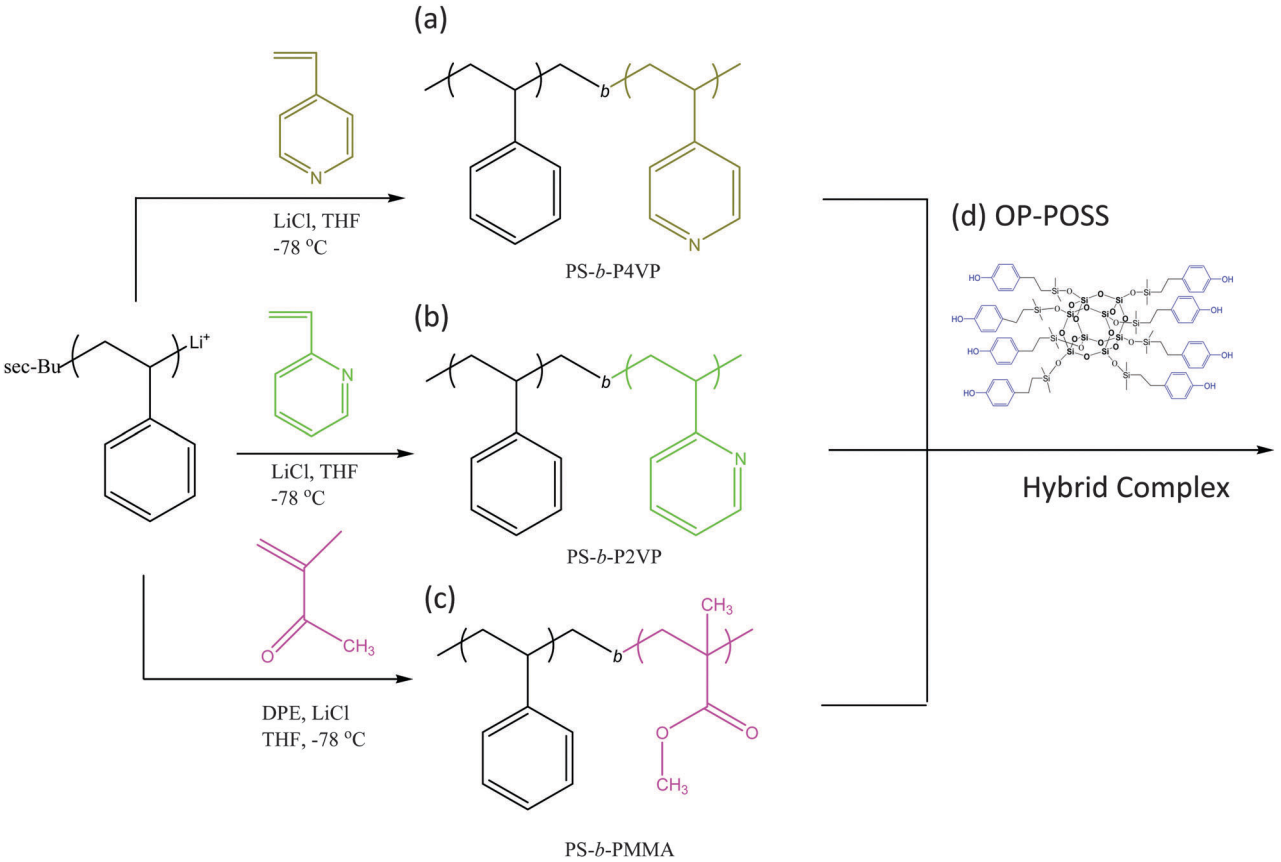

Scheme 1 The preparation of (a) PS-*b*-P4VP, (b) PS-*b*-P2VP, and (c) PS-*b*-PMMA through anionic polymerization; (d) the chemical structure of OP-POSS.

Table 1 Molecular weights (M_n), compositions (PS), polydispersity indices (PDIs), and glass transition temperature (T_g) of OP-POSS and PS-*b*-P4VP, PS-*b*-P2VP, and PS-*b*-PMMA BCPs

BCP[a]	M_n[b] (GPC)	PS[c] (wt%)	PDI[b]	T_g[d] (°C)
PS_{216}-*b*-$P4VP_{257}$	49 450	48	1.12	106/152
PS_{216}-*b*-$P2VP_{268}$	49 950	42	1.03	108/108
PS_{200}-*b*-$PMMA_{252}$	55 300	40	1.06	110/135
OP-POSS	1978	—	1.00	18

[a] Numbers denote final compositions determined through gel permeation chromatography (GPC, calibrated against polystyrene linear standards) and integrated ^{1}H NMR spectra. [b] Measured using GPC. [c] Determined from ^{1}H NMR spectra. [d] Determined from DSC analyses.

of PS blocks (106–116 °C) in these three BCPs are higher than PS homopolymer (~100 °C) of similar molecular weight due to the nano-confinement effect.

In Fig. 1(a), we also observe two values of T_g at relatively lower OP-POSS contents (< 50 wt%). Here, the lower value (85–106 °C) was assigned corresponding to the PS domain and the higher value (103–152 °C) was attributed to the hydrogen-bonded P4VP/OP-POSS complex domain. The single but broad T_g observed at *ca.* 86 °C was due to the T_g behavior of the PS domain, and P4VP/OP-POSS complex domain by coincidence decreased to the similar temperature range. Two T_g behaviors reappear at 80 wt% OP-POSS NPs from the P4VP/OP-POSS complex domain (63 °C) and the higher one (90 °C) corresponds to the PS domain.[41] In Fig. 1(b), although the pure PS-*b*-P2VP diblock copolymer and PS-*b*-P2VP/OP-POSS = 90/10 both displayed only the single glass transition temperature near 108 °C. Increasing to 20 wt% or more OP-POSS content shows two glass transition temperatures: the lower one (50–90 °C) from the hydrogen-bonded P2VP/OP-POSS domain and the higher one (100–108 °C) corresponding to the PS block segment. In Fig. 1(c), the pure PS-*b*-PMMA diblock copolymer also experienced two glass transition temperatures, but at 10 and 20 wt% of OP-POSS, we observed only a single glass transition temperature in each case, near 109 and 103 °C, respectively. The reason for this behavior is similar to that for PS-*b*-P4VP/OP-POSS complexes: the T_g of the PMMA/OP-POSS complex domain dropped to the similar glass transition temperature range of the PS domain. As a result, further increase in OP-POSS content to higher than 30 wt% also means two T_g values reappear again: the lower one (31–73 °C) corresponding to the PMMA/OP-POSS complex domain through hydrogen bonding and the higher one (95–102 °C) corresponding to the PS domain. In these three hybrid systems, we did not observe the single T_g for pure OP-POSS at 18 °C, indicating that no macrophase aggregation of OP-POSS NPs occurs due to the existing intermolecular hydrogen bonding between the phenolic hydroxyl (OH) groups of OP-POSS and the pyridine groups of P4VP/P2VP as well as the carbonyl (C=O) groups of PMMA.

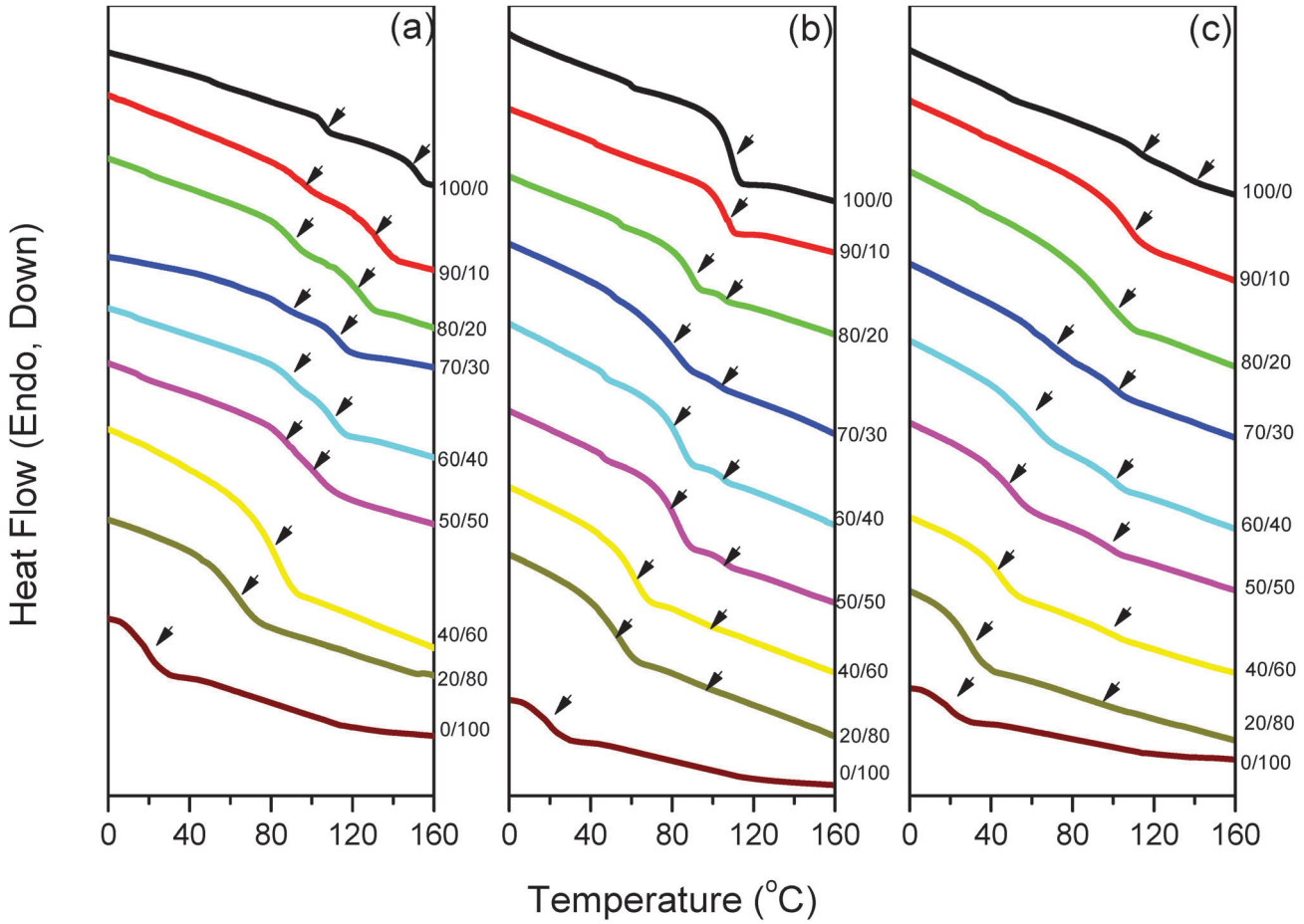

Fig. 1 DSC analyses of (a) PS-*b*-P4VP/OP-POSS, (b) PS-*b*-P2VP/OP-POSS, and (c) PS-*b*-PMMA/OP-POSS complexes.

Fig. 2 summarizes the T_g behavior of P4VP/OP-POSS, P2VP/OP-POSS, and PMMA/OP-POSS complex systems. Interestingly, the T_g behavior of the P4VP/OP-POSS and P2VP/OP-POSS complex domains exhibits the positive deviation compared with the linear rule, whereas that of the OP-POSS/PMMA complex domain exhibits the negative deviation. We employed the Kwei equation[52] to characterize specific interaction blending systems:

$$T_g = \frac{W_1 T_{g1} + k W_2 T_{g2}}{W_1 + k W_2} + q W_1 W_2 \quad (1)$$

where W_i and T_{gi} are the weight fractions and glass transition temperatures, respectively, of each component; k and q are the fitting constants. The values for the P4VP/OP-POSS complex (k = 1, q = 110) [Fig. 2(a)], the P2VP/OP-POSS complex (k = 1, q = 100) [Fig. 2(b)], and the PMMA/OP-POSS complex (k = 1, q = −50) [Fig. 2(c)] are obtained based on the non-linear least-squares best fitting. The positive q values suggest that the P4VP/OP-POSS and P2VP/OP-POSS complexes possess stronger inter-association hydrogen bonding than the self-association hydrogen bonding of OP-POSS. On the contrary, the inter-association hydrogen bonding of PMMA/OP-POSS complex is weaker than the self-association hydrogen bonding of OP-POSS, resulting in the negative q value. In addition, the q value of the P4VP/OP-POSS complex is larger than that of the P2VP/OP-POSS hybrid complex, because the steric hindrance affects the hydrogen bonding interaction strength.[50,53] Therefore, the hydrogen bonding interaction strengths in these systems follow the order of P4VP/OP-POSS > P2VP/OP-POSS > PMMA/OP-POSS, consistent with the values of K_A based on the Painter–Coleman

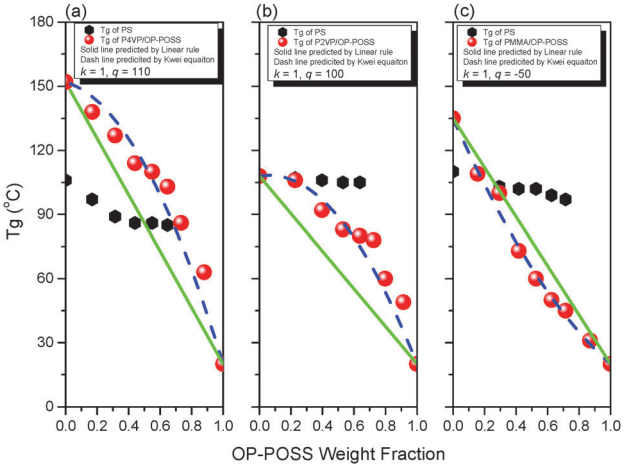

Fig. 2 T_g behavior of (a) PS-*b*-P4VP/OP-POSS, (b) PS-*b*-P2VP/OP-POSS, and (c) PS-*b*-PMMA/OP-POSS complexes.

association model: 1200 for P4VP/PVPh, 598 for P2VP/PVPh, and 37.4 for PMMA/PVPh.[46]

In addition, the T_g value of the PS block segment decreased with the increase of OP-POSS NPs content due to the lower T_g value of OP-POSS NPs.

Infrared spectroscopic analyses

Fig. 3 shows the infrared spectra of PS-*b*-P4VP/OP-POSS, PS-*b*-P2VP/OP-POSS, and PS-*b*-PMMA/OP-POSS complexes at room temperature. The OP-POSS possesses two major absorption peaks in the hydroxyl (OH) stretching region: one corresponding to the free hydroxyl group at 3525 cm^{-1} and the other broader band is centered at *ca.* 3350 cm^{-1} due to the self-association hydrogen-bonded hydroxyl–hydroxyl (OH–OH) groups. Clearly, the intensity of free hydroxyl groups of OP-POSS was decreased with the increase of PS-*b*-P4VP, PS-*b*-P2VP, and PS-*b*-PMMA contents. Moreover, the broad band peak was shifted to a relatively lower wavenumber with the increase of PS-*b*-P4VP and PS-*b*-P2VP contents, reflecting a redistribution of hydrogen bonds from self-association hydroxyl–hydroxyl interactions to inter-association hydroxyl–pyridine interactions, and thus we can assign the peak at 3150 cm^{-1} in Fig. 3(a) to the hydrogen bonding between the phenolic OH group of OP-POSS and the pyridine group of the P4VP block, and the band at 3190 cm^{-1} in Fig. 3(b) to the OH–pyridine interaction between OP-POSS and the P2VP block. In contrast, the broad signal for the hydrogen-bonded hydroxyl groups of OP-POSS was shifted to higher wavenumber (3430 cm^{-1}) at the highest PS-*b*-PMMA content (80 wt%) [Fig. 3(c)]. This phenomenon also suggests the new distribution of hydrogen bonds resulting from the competition between OH–OH of OP-POSS and OH–O=C of OP-POSS/PMMA complex. We used the frequency difference ($\Delta\nu$) between the free hydroxyl and intermolecular hydrogen bonded hydroxyl group signals to determine the average hydrogen bonding interaction strength[54] and found that the average hydrogen bonding interaction strength for both P4VP/OP-POSS ($\Delta\nu$ = 375 cm^{-1}) and P2VP/OP-POSS ($\Delta\nu$ = 335 cm^{-1}) were stronger than that from self-association of OH–OH for OP-POSS ($\Delta\nu$ = 185 cm^{-1}). As a result, the values of q are positive, based on the Kwei equation (Fig. 2). In contrast, the PMMA/OP-POSS ($\Delta\nu$ = 95 cm^{-1}) is weaker than self-association of OH–OH for OP-POSS, and thus the q value is negative, based on the Kwei equation (Fig. 2).

In addition to hydroxyl stretching, the pyridine groups of P4VP and P2VP and the carbonyl groups of PMMA are also sensitive to the hydrogen bonding interaction. In general, the band at 993 cm^{-1} characterizes the intermolecular hydrogen

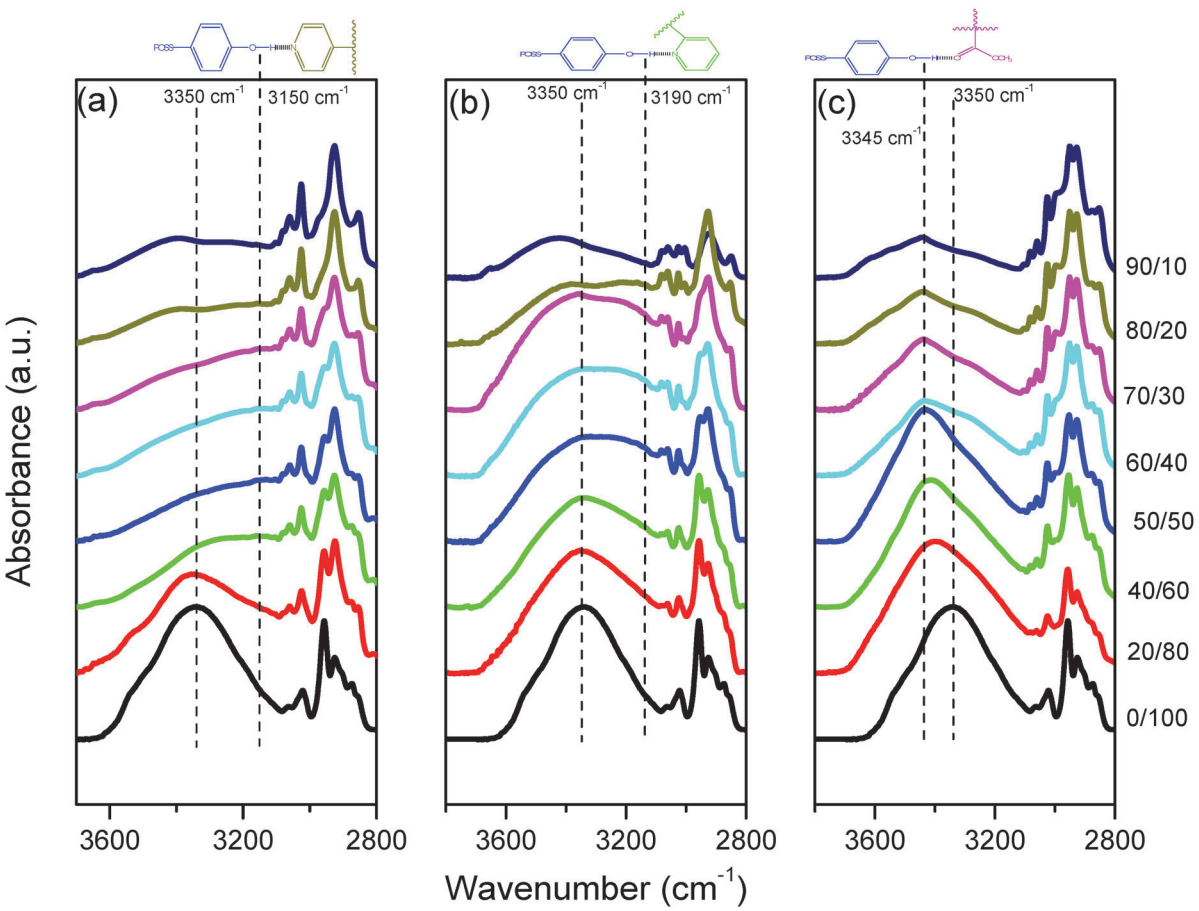

Fig. 3 FTIR spectra of the hydroxyl stretching region of (a) PS-*b*-P4VP/OP-POSS, (b) PS-*b*-P2VP/OP-POSS, and (c) PS-*b*-PMMA/OP-POSS complexes recorded at room temperature.

bonding of pyridine groups of the P4VP and P2VP block segments. Fig. 4(a) and (b) present infrared spectra in the range of 980–1020 cm^{-1} for PS-*b*-P4VP/OP-POSS and PS-*b*-P2VP/OP-POSS, respectively. Clearly, pure P4VP and P2VP blocks show the characteristic band at 993 cm^{-1} due to the free pyridine group. A new band was found at 1007 and 1005 cm^{-1} due to the hydrogen-bonded pyridine groups for the P4VP and P2VP block segments, respectively, when blending with OP-POSS NPs. We also found that the intermolecular hydrogen bonding strength in the P4VP/OP-POSS complex is stronger than that in the P2VP/OP-POSS complex because steric hindrance affects the specific interactions between these two polymers, as evidenced through different shifts in these frequencies (14 cm^{-1} for P4VP and 12 cm^{-1} for P2VP).[50] In addition, the band for the carbonyl group of PMMA block segment is split into two bands in Fig. 4(c): one at 1731 cm^{-1} is due to the free carbonyl groups in PS-*b*-PMMA and the other at 1710 cm^{-1} is due to the hydrogen-bonded ones. All pyridine and carbonyl group signals are split into two Gaussian bands that could be fitted well. Fig. 5 summarizes the curve fitting results, and we observed that the fraction of hydrogen-bonded pyridine groups of P4VP and P2VP and carbonyl groups of PMMA was increased upon increasing the OP-POSS content in these three hybrid complexes, which is similar to P4VP, P2VP, and PMA blending with phenolic resins.[50,55,56] In addition, Fig. 5 also shows that the fraction of hydrogen-bonded functional units also followed the order P4VP/OP-POSS > P2VP/OP-POSS > PMMA/OP-POSS, consistent with the DSC analyses. The hydrogen-bonded fraction in P4VP/OP-POSS was slightly higher than that in P2VP/OP-POSS, due to the effect of steric hindrance in these two hybrid systems.

SAXS and TEM analyses

Fig. 6 shows SAXS profiles of PS-*b*-P4VP/OP-POSS, PS-*b*-P2VP/OP-POSS, and PS-*b*-PMMA/OP-POSS blends with various compositions at room-temperature. The long-range order of the alternating lamellar structure was found for pure PS-*b*-P4VP [Fig. 6(a)] based on the scattering ratios with 1 : 2 : 3 : 4. The long period of this lamellar phase was *ca.* 45.1 nm based on the first SAXS peak at a position of q = 0.139 nm^{-1}, extracted from the $2\pi/q$ equation. The TEM image in Fig. 7(a) also shows the long-range order of alternating lamellar morphology for the pure PS-*b*-P4VP block possessing the alternating lamellar period *ca.* 40 nm, similar to the SAXS analysis shown in Fig. 6(a). On adding 10 or 20 wt% OP-POSS contents, more long range order of scattering peaks was observed compared with pure PS-*b*-P4VP, with peak ratios of 1 : 2 : 3 : 4 : 5 : 6 : 7 : 8, corresponding to the

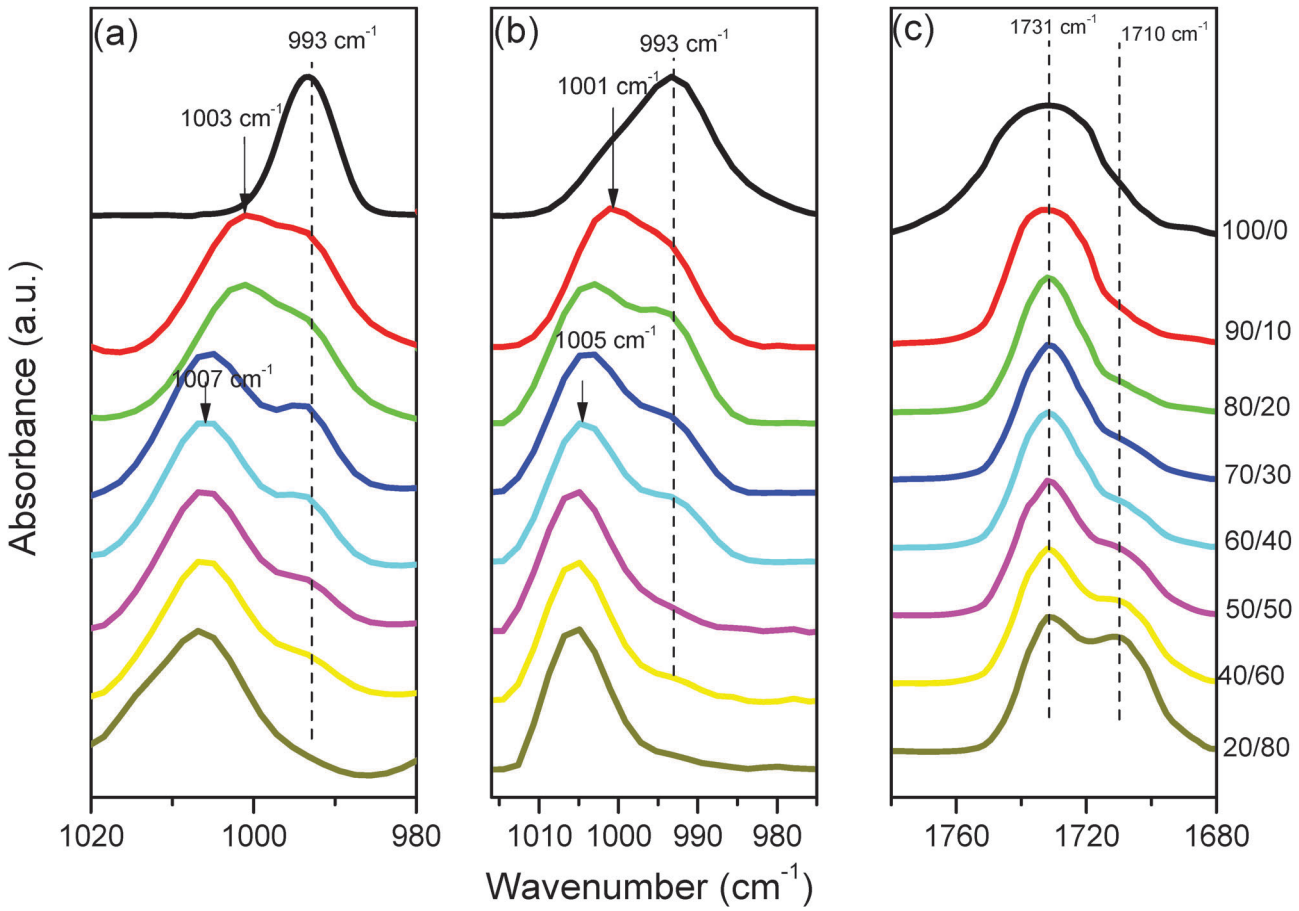

Fig. 4 FTIR spectra of (a) PS-*b*-P4VP/OP-POSS (pyridine region), (b) PS-*b*-P2VP/OP-POSS (pyridine region), and (c) PS-*b*-PMMA/OP-POSS (C=O region) hybrid complexes at room temperature.

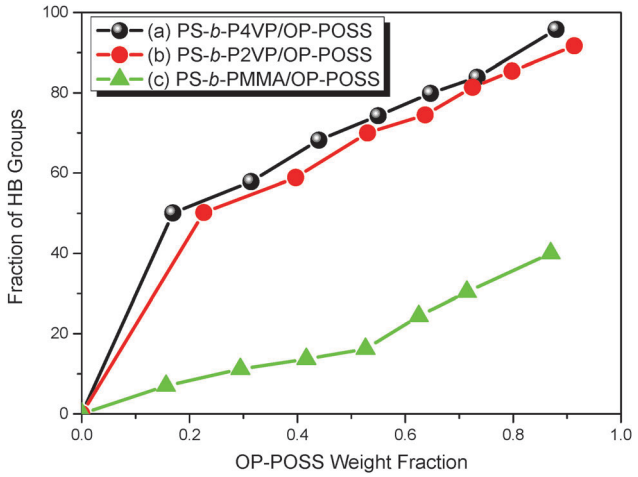

Fig. 5 Fractions of hydrogen-bonded functional groups of (a) PS-*b*-P4VP/OP-POSS (pyridine region), (b) PS-*b*-P2VP/OP-POSS (pyridine region), and (c) PS-*b*-PMMA/OP-POSS (C=O region) hybrid complexes.

lamellar structures, as confirmed by TEM images in Fig. 7(b) and (c). Furthermore, the first scattering peak was shifted to the lower q value slightly at 10 wt% OP-POSS content (q_{max} = 0.127 nm^{-1}; d = 49.4 nm), indicating an increase of the inter-lamellar spacing D. This peak was observed to shift to a higher q value at 20 wt% OP-POSS content (q_{max} = 0.151 nm^{-1}; d = 41.5). At 20 wt% composition, it transformed to a hexagonal packed cylindrical structure and further increasing to 30 wt% OP-POSS content, the morphology changed from alternating lamellar to hexagonal packed cylindrical structure with d = 41.5 nm. This order–order transition was due to the overall volume fraction change between these two diblock copolymer segments. The peak ratios did not change with the $1:\sqrt{3}:\sqrt{4}:\sqrt{7}:\sqrt{9}:\sqrt{12}$ ratio corresponding to long range order of hexagonal packed cylinder structures at 30, 40, and 50 wt% OP-POSS contents; this behavior was confirmed by TEM images shown in Fig. 7(d)–(f). The BCC symmetry spherical structure was observed as the OP-POSS content was at 60 and 80 wt% based on SAXS peaks with ratio of $1:\sqrt{2}:\sqrt{3}:\sqrt{4}$, consistent with the TEM image, as shown in Fig. 7(g) and (h). The order–order transition from alternating lamellae to hexagonally packed cylinders and finally to BCC spheres upon increasing OP-POSS content was observed based on SAXS and TEM analyses in the PS-*b*-P4VP/OP-POSS complex.

Similarly, SAXS analysis also shows the lamellar structure for the pure diblock copolymer of PS-*b*-P2VP [Fig. 6(b)], judging from the scattering peak ratio of 1:2:3:4. The SAXS peak located at the first q value of 0.131 nm^{-1} with d = 47.9 nm is for the lamellae structure. The PS volume fraction is 42% for this PS-*b*-P2VP diblock copolymer with the lamellar structure.

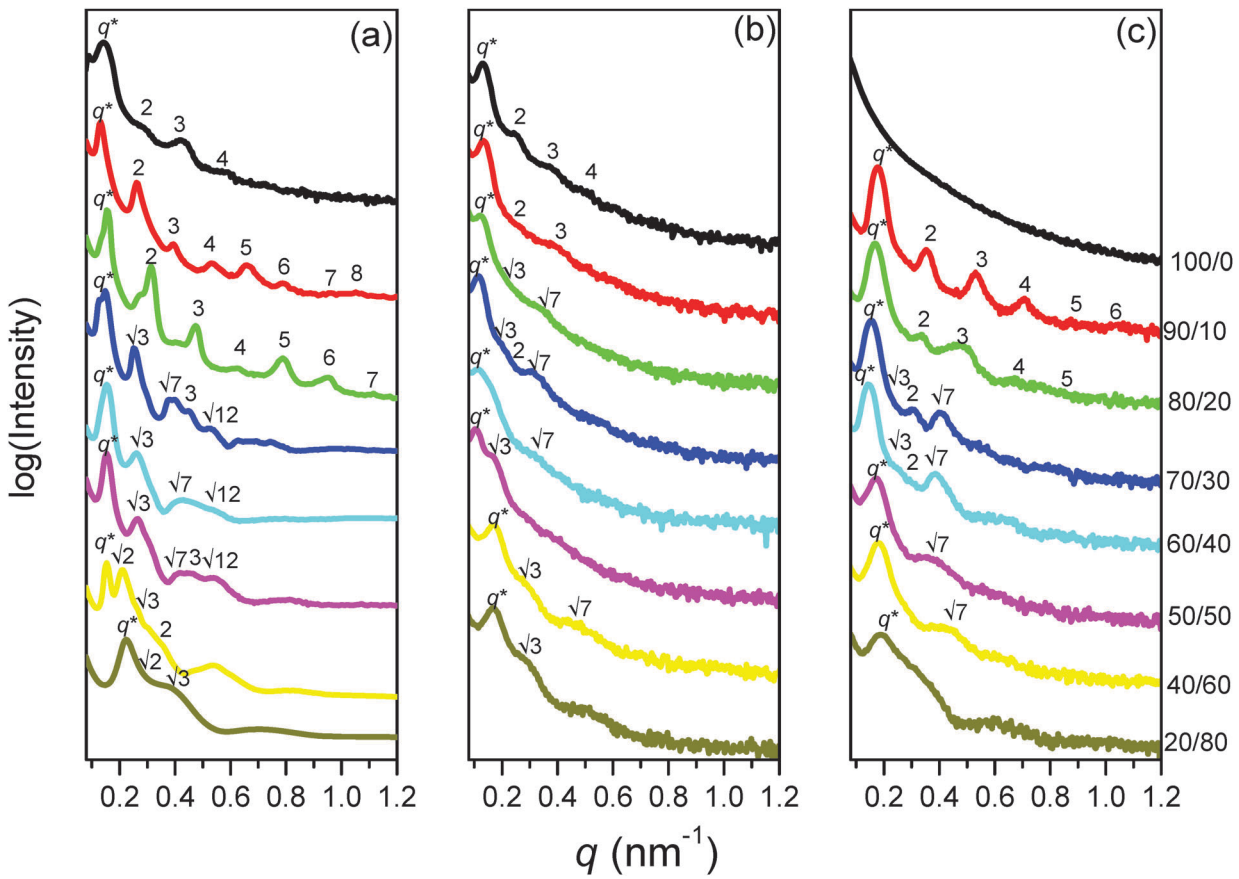

Fig. 6 SAXS patterns of (a) PS-*b*-P4VP/OP-POSS, (b) PS-*b*-P2VP/OP-POSS, and (c) PS-*b*-PMMA/OP-POSS hybrids at room temperature.

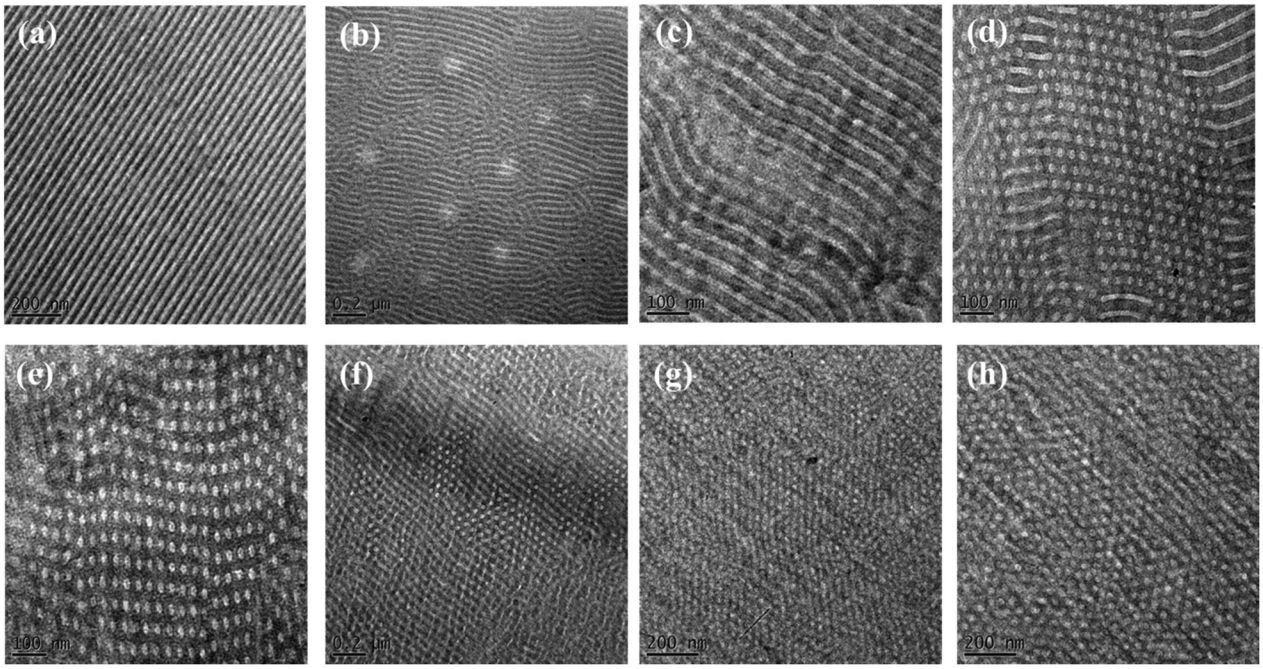

Fig. 7 TEM images of PS-*b*-P4VP/OP-POSS complex of (a) pure PS-*b*-P4VP, (b) 10, (c) 20, (d) 30, (e) 40, (f) 50, (g) 60, and (h) 80 wt% OP-POSS contents.

The TEM image in Fig. 8(a) shows that pure PS-*b*-P2VP diblock copolymer indeed exhibits the short-range ordered lamellar morphology. At 10 wt% OP-POSS content, the SAXS pattern retains this lamellar structure with a relative peak ratio of 1 : 2 : 3, as confirmed by the TEM image shown in Fig. 8(b). The first scattering peak was shifted to the low-q region slightly at 10 wt% OP-POSS (q_{max} = 0.129 nm^{-1}; d = 48.6 nm), also implying the increased d-spacing of inter-lamellae. By further increasing to 20–50 wt% OP-POSS content, the lamellar was transformed into the cylinders structure with d-spacings of 49.4, 53.2, 55.1, and 59.2 nm, respectively, which showed the $1:\sqrt{3}:\sqrt{4}:\sqrt{7}$ ratio for cylinder structures, as confirmed by TEM images in Fig. 8(c)–(f). On further increasing to 60 and 80 wt% OP-POSS content, the SAXS patterns show a ratio of $1:\sqrt{3}:\sqrt{7}$ and the d-spacings decrease to 37.4 nm (60 wt%) and 35.7 nm (80 wt%), implying the short-range ordered spherical micelle structure, as confirmed by the TEM images in Fig. 8(g) and (h), respectively. Similarly, the morphological transition

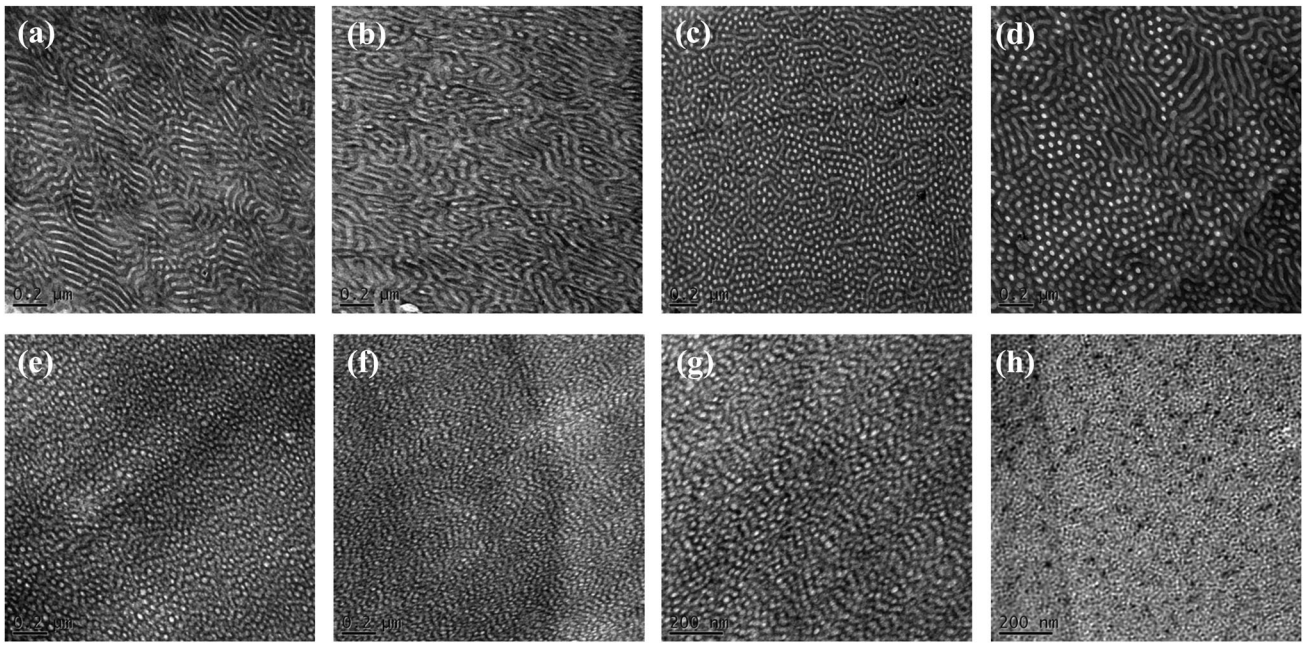

Fig. 8 TEM images of PS-*b*-P2VP/OP-POSS complex: (a) pure PS-*b*-P2VP, (b) 10, (c) 20, (d) 30, (e) 40, (f) 50, (g) 60, and (h) 80 wt% OP-POSS content.

also occurred with the increase of OP-POSS content in the PS-*b*-P2VP diblock copolymer. In contrast, because the hydrogen bonding in the P2VP/OP-POSS complexes was weak relative to the P4VP/OP-POSS complexes, the former system formed disordered structures at relatively higher OP-POSS content (>60 wt%).

SAXS analysis showed a disordered and phase-mixed structure for pure PS-*b*-PMMA [Fig. 6(c)]; TEM imaging supported the presence of a phase-mixed structure [Fig. 9(a)]. It is well established that PS-*b*-PMMA diblock copolymers show an upper disorder–order transition (UDOT) and that the the interaction parameter (χ) is quite weak.[57,58] In addition, the degree of polymerization (N = 452) of the PS-*b*-PMMA diblock copolymer used in this study was not particularly high; thus, at low values of χN, the PS-*b*-PMMA was phase-mixed.[57,58] Nevertheless, after adding 10 wt% OP-POSS content into the PS-*b*-PMMA (7% of C═O groups interacted with OP-POSS), sharp scattering patterns appeared with a relative peak ratio of 1 : 2 : 3 : 4 : 5 : 6, having the long period of lamellar structure of 35.2 nm; the TEM image in Fig. 9(b) confirmed such a structure. On further increasing to 20 wt% OP-POSS content (11.2% of C═O groups interacted with OP-POSS), the scattering pattern remained sharp with a relative peak ratio of 1 : 2 : 3 : 4 : 5, also suggesting the long-range ordered lamellar structures, as confirmed by the TEM image in Fig. 9(c). The first scattering peak was also slightly shifted to the low-q region (q_{max} = 0.165 nm^{-1}; d = 38.0 nm), again implying the increased d-spacing of interlamellae. Russell *et al.* have reported the increase of segmental interaction parameter (χ) between PS and PMMA due to the formation of PMMA–lithium ionic complexes; they also found that the PS-*b*-PMMA diblock copolymer shows morphology from the phase-mixed to the microphase-separation structure after the formation of PMMA–lithium ionic complexes.[59,60]

In this study, intermolecular hydrogen bonding existed between the phenolic hydroxyl groups of OP-POSS and the carbonyl groups of PMMA, which also increased the segmental interaction parameter between PS and PMMA and effectively increased molecular weight by physical cross-linking through hydrogen bonding and, therefore, increased the value of χN. As a result, we found that the change in morphology from a phase-mixed to a long-range-ordered lamellar structure occurred when only 10 or 20 wt% OP-POSS was added. On further increasing the OP-POSS content to 30 and 40 wt%, the transition occurred from the alternating lamellar to the cylinder structure with the d-spacings of 39.0 and 43.3 nm, respectively, as revealed from the $1:\sqrt{3}:\sqrt{4}:\sqrt{7}$ ratio expected for cylindrical structures; the TEM images in Fig. 9(d) and (e) confirmed this behavior. Further increasing the OP-POSS NP content to 50 and 60 wt%, the SAXS patterns showed a ratio of $1:\sqrt{7}$ and the d-spacings decreased to 36.3 nm (50 wt%) and 34.5 nm (60 wt%), indicating that the morphologies of these samples featured short-range ordered wormlike structures, as confirmed by the TEM images in Fig. 9(f) and (g), respectively. When the OP-POSS content was 80 wt%, a broad peak was formed, with the d-spacing decreasing further to 31.5 nm, corresponding to a disordered micelle or macrophase-separated structure, as confirmed by the TEM image shown in Fig. 9(h).

The distributions of OP-POSS NPs in these three complexes were investigated in this study. The average distance a_J for the chemical junction of the block copolymer interface and the relative changes of a_J/a_{J0} were derived for the complexes, where a_{J0} corresponds to the pure diblock copolymer. The values of D/D_0 of $(\rho_J/\rho_{J0})\Phi_{block}{}^{-1}$ are simple volumetric conversion for the lamellar strucutre, $(\rho_J/\rho_{J0})[(2/3^{1/2})\pi(1-f)\Phi_{block}{}^{-1}]^{1/2}$ for the cylindrical structure, and $(\rho_J/\rho_{J0})\left[(27\sqrt{3}/8)\pi(1-f)^2\Phi_{block}{}^{-1}\right]^{1/2}$

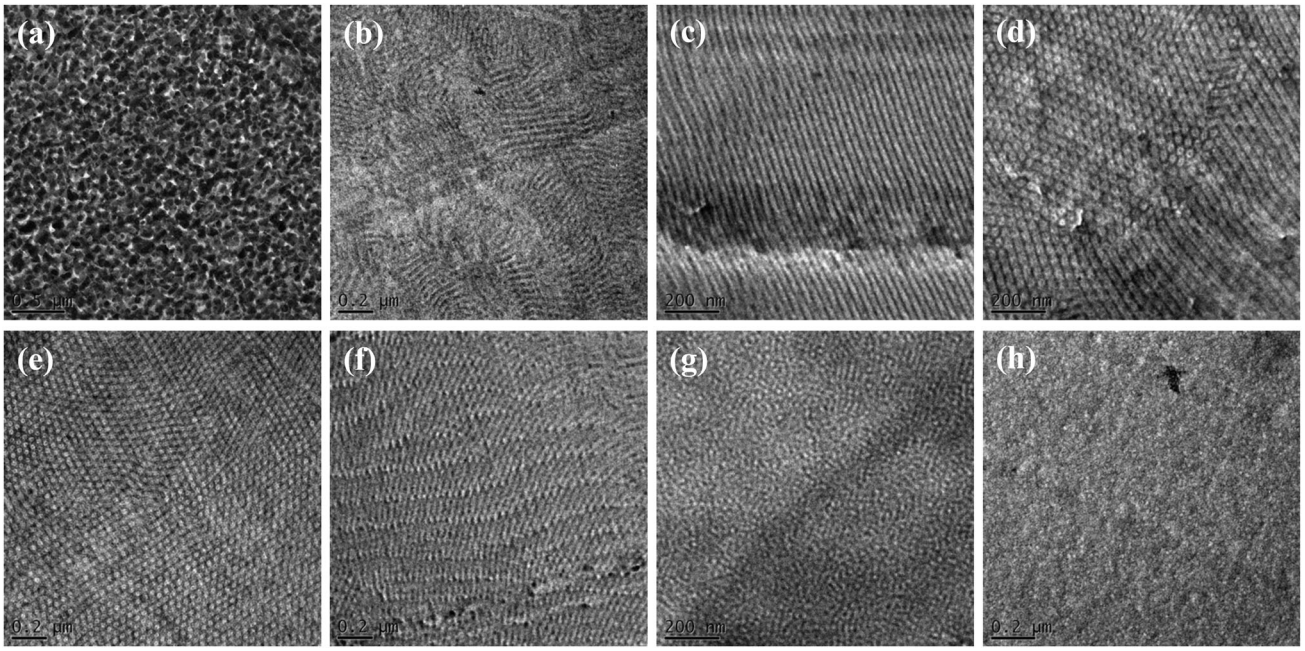

Fig. 9 TEM images of PS-*b*-PMMA/OP-POSS complex of (a) pure PS-*b*-PMMA, (b) 10, (c) 20, (d) 30, (e) 40, (f) 50, (g) 60, and (h) 80 wt% OP-POSS contents.

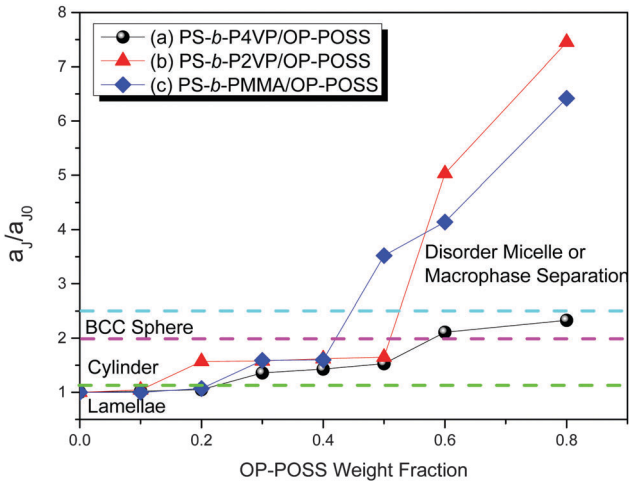

Fig. 10 Average distances of the chemical junctions along the interface, a_J/a_{J0}, for (a) PS-*b*-P4VP/OP-POSS, (b) PS-*b*-P2VP/OP-POSS, and (c) PS-*b*-PMMA/OP-POSS complexes.

for the body-centered cubic spherical structure. D_0 is the inter-distance of pure diblock copolymer, f is the PS block volume fraction, and ρ_J corresponds to the block chain number per unit interfacial area (a_J^2); thus, a_J/a_{J0} is equal to $(\rho_J/\rho_{J0})^{-1/2}$ and Φ is the volume fraction of BCPs in the complexes.[31,32] Fig. 10 summarizes the a_J/a_{J0} values in these three hybrid systems with various OP-POSS contents based on the abovementioned three relationships. We observed the expansion in the a_J values ($a_J/a_{J0} > 1$) for all three hybrid systems—presumably the result of the additive OP-POSS intervening and wetting the P4VP, P2VP, and PMMA chains of the BCPs at the interfaces through hydrogen bonding. We consider no change in BCP/NPs density because the PS block covalently linked to the hydrogen bonded acceptor blocks P4VP, P2VP, and PMMA segments, which have to contract to accommodate the expanded interfacial zone.

The values of a_J/a_{J0} for the P4VP/P4VP complexes increased from 1.02 (at 10 wt% OP-POSS) to 2.35 (at 80 wt% OP-POSS). Scheme 2(a) summarizes the morphological transformation of PS-*b*-P4VP that occurred upon increasing the OP-POSS content. Pure PS-*b*-P4VP shows the long-range order of the alternating lamellar structure on increasing the OP-POSS content to 10 and 20 wt% and retains the lamellar structure. On further increasing the OP-POSS content to 30–50 wt%, the structures changed to cylindrical with corresponding increase in *d*-spacing, with values of a_J/a_{J0} of 1.35, 1.42, and 1.52 for the blends having OP-POSS contents of 30, 40, and 50 wt%, respectively. At 60 wt% and 80 wt% OP-POSS content, BCC spheres were formed and the *d*-spacing decreased significantly, providing values of a_J/a_{J0} of 2.06 and 2.35, respectively. This order–order transition from lamellae to cylinder and finally to BCC sphere comes from the relatively stronger hydrogen bonding interaction between the phenolic hydroxyl groups of OP-POSS and the pyridine groups of P4VP, which changes the overall volume fractions of block copolymer segments.

Scheme 2(b) summarizes the morphological transformation of PS-*b*-P2VP diblock copolymer upon increasing the OP-POSS content. Pure PS-*b*-P2VP shows a lamellar structure; at 10 wt% OP-POSS NP content, the lamellar structure was maintained, with an a_J/a_{J0} value of 1.04. With the OP-POSS content at 20–50 wt%, the composition changed to cylindrical structures with corresponding increases in the *d*-spacing and a_J/a_{J0} values of 1.57, 1.58, 1.62, and 1.65 at OP-POSS contents of 20, 30, 40, and 50 wt%, respectively. On further increasing OP-POSS NP content to 60 and 80 wt%, the *d*-spacings decreased, with the a_J/a_{J0} values increasing significantly to 5.03 and 7.45, respectively, when using the sphere model. This phenomenon could be explained as the result of a short-range ordered spherical micelle structure forming at these compositions; the curvature changed significantly and then increased the a_J/a_{J0} value. Because the hydrogen bonding in PS-*b*-P2VP/OP-POSS complexes was weaker than that of P4VP/OP-POSS complexes, due to the steric hindrance effect, the former system formed close-to-disordered structures at relatively higher OP-POSS contents (>60 wt%).

Scheme 2(c) also summarizes the morphological transformation of PS-*b*-PMMA upon increasing the OP-POSS content. Pure PS-*b*-PMMA shows a phase-mixed structure because of the lower value of χN. When the OP-POSS NP contents were at 10 and 20 wt%, the phase-mixed structure changed to the long-range order of alternating lamellar structures because of hydrogen bonding interaction between the phenolic hydroxyl groups of OP-POSS and the carbonyl groups of PMMA and thus increased the interaction parameter between PS and PMMA block segments and then increased the value of χN. Because the pure PS-*b*-PMMA diblock copolymer possessed a phase-mixed structure, we could not determine a value of D_0. For comparison, we chose a value of D_0 of 35.2 nm for the 10 wt% OP-POSS content system in PS-*b*-PMMA; thus, the value of a_J/a_{J0} was 1.07 for the system containing 20 wt% OP-POSS. On further increasing the OP-POSS content to 30–40 wt%, the structures became cylindrical with corresponding increases in *d*-spacings, with a_J/a_{J0} values of 1.59 and 1.60 at OP-POSS contents of 30 and 40 wt%, respectively. When the OP-POSS NP contents were 50, 60, and 80 wt%, the *d*-spacings decreased and the values of a_J/a_{J0} increased significantly to 3.52, 4.14, and 6.42, respectively, when using the sphere model. This phenomenon can be explained as arising from short-range-ordered spherical micelles or macrophase-separated structures at these compositions. Because the PS-*b*-PMMA/OP-POSS complexes experienced the weakest hydrogen bonding among these three systems, they formed close-to-disordered structures at only 50 wt% OP-POSS content.

In summary, at relatively low OP-POSS contents (*ca.* 10–20 wt%), all these hybrid systems almost formed lamellar structures with lower a_J/a_{J0} values (<1.07), with the OP-POSS NPs displaying wet-brush behavior for each of these three diblock copolymers. When the OP-POSS content was approximately 30–40 wt%, order-order transition behavior occurred, from lamellar to hexagonally packed cylinder structures, with a_J/a_{J0} values between 1.35 and 1.65, because the overall volume fractions of block copolymer segments were changed by hydrogen bonding interactions. On further increasing the OP-POSS content to approximately 50–80 wt% (higher OP-POSS contents), the self-assembled structures that were formed were strongly dependent on the hydrogen bonding strength. For example, the system featuring

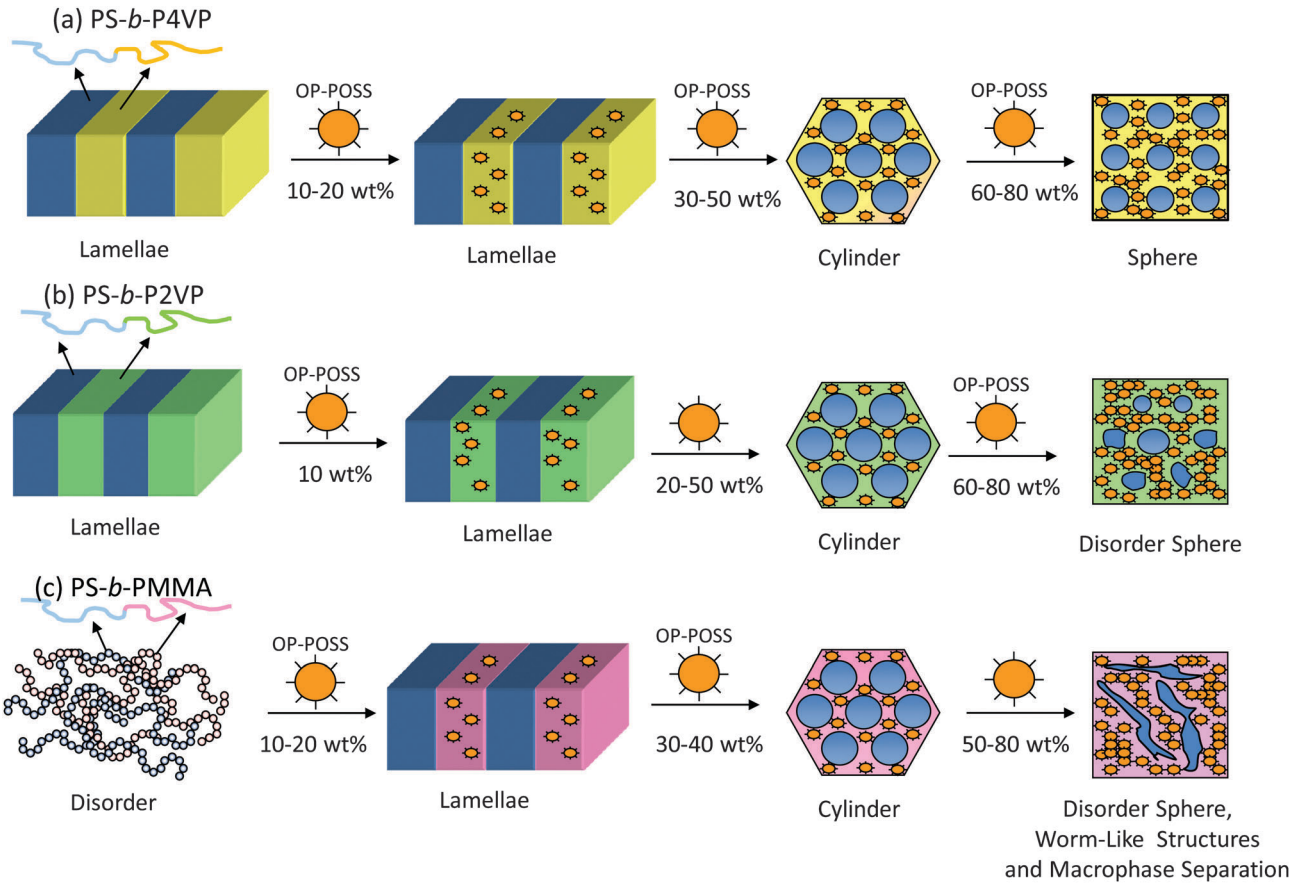

Scheme 2 Morphological transitions of (a) PS-*b*-P4VP/OP-POSS, (b) PS-*b*-P2VP/OP-POSS, and (c) PS-*b*-PMMA/OP-POSS complexes with the increase of OP-POSS contents.

the strongest hydrogen bonds, namely, the PS-*b*-P4VP/OP-POSS complex, underwent an additional order–order transition to form BCC spheres at an 80 wt% OP-POSS content, with a relatively low a_J/a_{J0} value (2.35). The PS-*b*-PMMA/OP-POSS complex, featuring the weakest hydrogen bonds, had already formed a disordered structure at only 50 wt% OP-POSS content. Consistent with this behavior, the PS-*b*-P2VP/OP-POSS hybrid complexes displayed their disordered structure at 60 wt% OP-POSS content.

Conclusions

In this study, the phase behavior, hydrogen bonding interactions, and self-assembly structures of PS-*b*-P4VP/OP-POSS, PS-*b*-P2VP/OP-POSS, and PS-*b*-PMMA/OP-POSS complexes were investigated in detail by DSC, TEM, SAXS, and FTIR spectroscopy. The self-assembly structure of block copolymer composites with OP-POSS was strongly dependent on the functional group polarity of block segments. The relatively weaker intermolecular hydrogen bonding in the PS-*b*-P2VP/OP-POSS and PS-*b*-PMMA/OP-POSS complexes in block copolymer formed close-to-disordered structures at relatively higher OP-POSS contents. In contrast, the strongest hydrogen bonding interaction in the PS-*b*-P4VP/OP-POSS complex induced the order–order transition from alternating lamellae to cylinders and finally to BCC spheres. We conclude that the hydrogen bonding strength, and not the BCP composition, is the key feature affecting the types of self-assembled structures that were formed in this study.

Acknowledgements

This study was supported financially by the Ministry of Science and Technology, Republic of China, under contracts MOST 100-2221-E-110-029-MY3 and MOST 102-2221-E-110-008-MY3. We thank Mr Hsien-Tsan Lin of the Regional Instruments Center at National Sun Yat-Sen University for help with the TEM experiments.

References

1 L. Zhang, H. Li and L. Wu, *Soft Matter*, 2014, **10**, 6791–6797.
2 J. Rodriguez-Hernandez, F. Checot, Y. Gnanou and S. Lecommandoux, *Prog. Polym. Sci.*, 2005, **30**, 691–724.
3 C. Sanchez, K. J. Shea and S. Kitagawa, *Chem. Soc. Rev.*, 2011, **40**, 471–472.

4 J. Pyun and K. Matyjaszewski, *Chem. Mater.*, 2001, **13**, 3436–3448.
5 K. Zhang, L. Gao and Y. Chen, *Macromolecules*, 2007, **40**, 5916–5922.
6 J. G. Son, A. F. Hannon, K. W. Gotrik, A. Alexander-Katz and C. A. Ross, *Adv. Mater.*, 2011, **23**, 634–639.
7 D. Borah, M. Ozmen, S. Rasappa, M. T. Shaw, J. D. Holmes and M. A. Morris, *Langmuir*, 2013, **29**, 2809–2820.
8 T. Hirai, M. Leolukman, S. Jin, R. Goseki, Y. Ishida, M. Kakimoto, T. Hayakawa, M. Ree and P. Gopalan, *Macromolecules*, 2009, **42**, 8835–8843.
9 T. Hirai, M. Leolukman, C. C. Liu, E. Han, Y. J. Kim, Y. Ishida, T. Hayakawa, M. Kakimoto, P. F. Nealey and P. Gopalan, *Adv. Mater.*, 2009, **21**, 4334–4338.
10 C. W. Chiou, Y. C. Lin, T. Hayakawa and S. W. Kuo, *Macromolecules*, 2014, **47**, 8709–8721.
11 Y. C. Wu and S. W. Kuo, *J. Mater. Chem.*, 2012, **22**, 2982–2991.
12 S. W. Kuo and F. C. Chang, *Prog. Polym. Sci.*, 2011, **36**, 1649–1696.
13 X. Yu, K. Yue, I. F. Hsieh, Y. Li, X. H. Dong, Y. Xin, H. F. Wang, A. C. Shi, G. R. Newkome, R. M. Ho, E. Q. Chen, W. B. Zhang and S. Z. D. Cheng, *Proc. Natl. Acad. Sci. U. S. A.*, 2013, **110**, 10078–10083.
14 W. B. Zhang, X. Yu, C. L. Wang, H. J. Sun, I. F. Hsieh, Y. Li, X. H. Dong, K. Yue, R. V. Horn and S. Z. D. Cheng, *Macromolecules*, 2014, **47**, 1221–1239.
15 S. G. Jang, E. J. Kramer and C. J. Hawker, *J. Am. Chem. Soc.*, 2011, **133**, 16986–16996.
16 Y. Lin, V. K. Daga, E. R. Anderson, S. P. Gido and J. J. Watkins, *J. Am. Chem. Soc.*, 2011, **133**, 6513–6516.
17 V. K. Daga, E. R. Anderson, S. P. Gido and J. J. Watkins, *Macromolecules*, 2011, **44**, 6793–6799.
18 A. Noro, K. Higuchi, Y. Sageshima and Y. Matsushita, *Macromolecules*, 2012, **45**, 8013–8020.
19 S. G. Jang, A. Khan, C. J. Hawker and E. J. Kramer, *Macromolecules*, 2012, **45**, 1553–1561.
20 T. Lin, R. M. Ho and J. C. Ho, *Macromolecules*, 2009, **42**, 742–751.
21 (*a*) V. Ramna, R. Sharma, T. A. Hatton and B. D. Olsen, *ACS Macro Lett.*, 2013, **2**, 655–659; (*b*) W. Zoelen, A. H. G. Vlooswijk, A. Ferri, A. M. Andringa, B. Noheda and t.-G. Brinke, *Chem. Mater.*, 2009, **21**, 4719–4723; (*c*) K. Thorkelsson, A. J. Mastroianni, P. Ercuius and T. Xu, *Nano Lett.*, 2012, **12**, 498–504; (*d*) J. Kao, K. Thorkelsson, P. Bai, B. J. Rancatore and T. Xu, *Chem. Soc. Rev.*, 2013, **42**, 2654–2678.
22 A. C. Balazs, T. Emrick and T. P. Russell, *Science*, 2006, **314**, 1107–1110.
23 J. Y. Cheng, C. A. Ross, V. Z. H. Chan, E. L. Thomas, R. G. H. Lammertink and G. J. Vancso, *Adv. Mater.*, 2001, **13**, 1174–1178.
24 T. F. Jaramillo, S. H. Baeck, B. R. Cuenya and E. W. McFarland, *J. Am. Chem. Soc.*, 2003, **125**, 7148–7149.
25 B. Sarkar and P. Alexandridis, *Langmuir*, 2012, **28**, 15975–15986.
26 J. J. Chiu, B. J. Kim, E. J. Kramer and D. J. Pine, *J. Am. Chem. Soc.*, 2005, **127**, 5036–5037.
27 B. J. Kim, J. Bang, C. J. Hawker and E. J. Kramer, *Macromolecules*, 2006, **39**, 4108–4114.
28 S. C. Park, B. J. Kim, C. J. Hawker, E. J. Kramer, J. Bang and J. S. Ha, *Macromolecules*, 2007, **40**, 8119–8124.
29 J. J. Chiu, B. J. Kim, G. R. Yi, J. Bang, E. J. Kramer and D. J. Pine, *Macromolecules*, 2007, **40**, 3361–3365.
30 B. J. Kim, G. H. Fredrickson and E. J. Kramer, *Macromolecules*, 2008, **41**, 436–447.
31 T. Hashimoto, H. Tanaka and H. Hasegawa, *Macromolecules*, 1990, **023**, 4378–4386.
32 T. Tanaka, H. Hasegawa and T. Hashimoto, *Macromolecules*, 1991, **24**, 240–251.
33 U. S. Jeng, Y. S. Sun, H. J. Lee, C. H. Hsu, K. S. Liang, S. W. Yeh and K. H. Wei, *Macromolecules*, 2004, **37**, 4617–4622.
34 S. W. Yeh, K. H. Wei, Y. S. Sun, U. S. Jeng and K. S. Liang, *Macromolecules*, 2003, **36**, 7903–7907.
35 S. W. Yeh, K. H. Wei, Y. S. Sun, U. S. Jeng and K. S. Liang, *Macromolecules*, 2005, **38**, 6559–6565.
36 C. H. Lu, S. W. Kuo, W. T. Chang and F. C. Chang, *Macromol. Rapid Commun.*, 2009, **30**, 2121–2127.
37 S. W. Kuo and H. Y. Yang, *Macromol. Chem. Phys.*, 2011, **212**, 2249–2259.
38 Y. R. Wu, Y. C. Wu and S. W. Kuo, *Macromol. Chem. Phys.*, 2013, **214**, 1496–1503.
39 M. Ramanathan, S. M. Killbey, Q. Ji, J. P. Hill and K. Ariga, *J. Mater. Chem.*, 2012, **22**, 10389–10405.
40 W. Ding, J. Lin, K. Yao, J. W. Mays, M. Ramanathan and K. Hong, *J. Mater. Chem. B*, 2013, **1**, 4212–4216.
41 Y. S. Lu and S. W. Kuo, *RSC Adv.*, 2014, **4**, 34849–34859.
42 S. C. Chen, S. W. Kuo, U. S. Jeng, C. J. Su and F. C. Chang, *Macromolecules*, 2010, **43**, 1083–1092.
43 M. M. Coleman, J. F. Graf and P. C. Painter, *Specific Interactions and the Miscibility of Polymer Blends*, Technomic Publishing, Lancaster, PA, 1991.
44 C. L. Lin, W. C. Chen, C. S. Liao, Y. C. Su, C. F. Huang, S. W. Kuo and F. C. Chang, *Macromolecules*, 2005, **38**, 6435–6444.
45 S. W. Kuo, P. H. Tung and F. C. Chang, *Macromolecules*, 2006, **39**, 9388–9395.
46 Y. C. Sheen, C. H. Lu, C. F. Huang, S. W. Kuo and F. C. Chang, *Polymer*, 2008, **49**, 4017–4024.
47 Y. J. Yen, S. W. Kuo, C. F. Huang, J. K. Chen and F. C. Chang, *J. Phys. Chem. B*, 2008, **112**, 10821–10829.
48 K. W. Huang, L. W. Tsai and S. W. Kuo, *Polymer*, 2009, **50**, 4876–4887.
49 S. W. Kuo, H. C. Lin, W. J. Huang, C. F. Huang and F. C. Chang, *J. Polym. Sci., Part B: Polym. Phys.*, 2006, **44**, 673–686.
50 S. W. Kuo, C. L. Lin and F. C. Chang, *Polymer*, 2002, **43**, 3943–3949.
51 C. Tsitsilianis and G. Staikos, *Macromolecules*, 1992, **25**, 910–916.
52 T. K. Kwei, *J. Polym. Sci., Polym. Lett. Ed.*, 1984, **22**, 307–313.

53 S. W. Kuo, C. H. Wu and F. C. Chang, *Macromolecules*, 2004, **37**, 192–200.
54 S. W. Kuo, *J. Polym. Res.*, 2008, **15**, 459–486.
55 C. F. Huang, S. W. Kuo, H. C. Lin, J. K. Chen, Y. K. Chen, H. Y. Xu and F. C. Chang, *Polymer*, 2004, **45**, 5913–5921.
56 C. F. Huang, S. W. Kuo, F. J. Lin, W. J. Huang, C. F. Wang, W. Y. Chen and F. C. Chang, *Macromolecules*, 2006, **39**, 300–308.
57 J. Holoubek, F. Lednicky and J. Baldrian, *Eur. Polym. J.*, 2006, **42**, 2236–2246.
58 A. V. G. Ruzette, A. M. Mayes, M. Pollard, T. P. Russell and B. Hammouda, *Macromolecules*, 2003, **36**, 3351–3356.
59 J. Y. Wang, W. Chen, C. Roy, J. D. Sievert and T. P. Russell, *Macromolecules*, 2008, **41**, 963–969.
60 J. Y. Wang, W. Chen and T. P. Russell, *Macromolecules*, 2008, **41**, 4904–4907.

